

Comparing the Convective Structure and Microphysics in Two Sahelian Mesoscale Convective Systems: Radar Observations and CRM Simulations

NICK GUY*

Department of Atmospheric Science, Colorado State University, Fort Collins, Colorado

XIPING ZENG

Laboratory for Atmospheres, NASA Goddard Space Flight Center, Greenbelt, and Goddard Earth Sciences Technology and Research, Morgan State University, Baltimore, Maryland

STEVEN A. RUTLEDGE

Department of Atmospheric Science, Colorado State University, Fort Collins, Colorado

WEI-KUO TAO

Laboratory for Atmospheres, NASA Goddard Space Flight Center, Greenbelt, Maryland

(Manuscript received 19 February 2012, in final form 1 August 2012)

ABSTRACT

Two mesoscale convective systems (MCSs) observed during the African Monsoon Multidisciplinary Analyses (AMMA) experiment are simulated using the three-dimensional (3D) Goddard Cumulus Ensemble model. This study was undertaken to determine the performance of the cloud-resolving model in representing distinct convective and microphysical differences between the two MCSs over a tropical continental location. Simulations are performed using 1-km horizontal grid spacing, a lower limit on current embedded cloud-resolving models within a global multiscale modeling framework. Simulated system convective structure and microphysics are compared to radar observations using contoured frequency-by-altitude diagrams (CFADs), calculated ice and water mass, and identified hydrometeor variables. Vertical distributions of ice hydrometeors indicate underestimation at the mid- and upper levels, partially due to the inability of the model to produce adequate system heights. The abundance of high-reflectivity values below and near the melting level in the simulation led to a broadening of the CFAD distributions. Observed vertical reflectivity profiles show that high reflectivity is present at greater heights than the simulations produced, thought to be a result of using a single-moment microphysics scheme. Relative trends in the population of simulated hydrometeors are in agreement with observations, though a secondary convective burst is not well represented. Despite these biases, the radar-observed differences between the two cases are noticeable in the simulations as well, suggesting that the model has some skill in capturing observed differences between the two MCSs.

1. Introduction

During the West African monsoon (June–September), mesoscale convective systems (MCSs) provide the majority of precipitation in West Africa (Le Barbé and Lebel

1997; D’Amato and Lebel 1998; Laurent et al. 1998; Mathon et al. 2002; Redelsperger et al. 2002; Fink et al. 2006), often taking the form of squall lines (Hamilton et al. 1945; Eldridge 1958; Bolton 1984; Houze et al. 1989), a highly organized type of system that primarily exhibits a leading convective line with cirriform anvil preceding an extensive trailing, precipitating stratiform cloud. Two-way interactions with the major synoptic feature, African easterly waves (AEWs), have been shown. Modulation of the evolution (Payne and McGarry 1977; Machado et al. 1993) and generation (Fink et al. 2006) of MCSs may occur in the presence of AEWs,

* Current affiliation: NOAA/National Severe Storms Laboratory, Norman, Oklahoma.

Corresponding author address: Nick Guy, NOAA/NSSL/WRDD, 120 David L. Boren Blvd., Norman, OK 73072.
E-mail: nick.guy@noaa.gov

along with the modification of the large-scale environment through moisture (Lafore et al. 1988) and momentum (Moncrieff 1992) transport or reinforcement of cyclonic rotation (Barthe et al. 2010).

A few studies note the existence of MCSs with no association to AEWs (Fink et al. 2006; Laing et al. 2008, Guy et al. 2011). Analysis of ground-based radar data at continental, coastal, and maritime locations revealed that regional differences in convective characteristics were more apparent than differences between AEWs and no-wave events (Guy et al. 2011); however, the system structure and duration exhibited variations according to synoptic–dynamic and local thermodynamic forcing. A climatological analysis using 13 yr of Tropical Rainfall Measuring Mission (TRMM) data (precipitation radar and microwave) showed differences in stratiform fractions, microphysics, and ice and liquid water mass when subdivided by AEW phase and when no wave was present (Guy and Rutledge 2012).

Numerical weather prediction models have historically performed poorly in representing characteristics of the West African monsoon (WAM); see Ruti et al. (2011) for an overview of key results to date. Recent studies have indicated that improved forecasts and simulations were obtained with the ingestion of additional observational data (Tompkins et al. 2005; Faccani et al. 2009; Agustí-Panareda et al. 2010), though the impact of the additional information disappeared within 1 day (Agustí-Panareda et al. 2010). Despite better intraseasonal representations of AEWs in the latest generation of global climate models (GCMs), challenges still exist in understanding the mechanisms driving the discrepancies (Ruti et al. 2011). Even with improvements in the representation of AEWs and other synoptic features, shorter-time-scale (smaller spatial scale) variability (e.g., precipitation) is less reproducible in simulations (e.g., Vanvyve et al. 2008).

Multiscale model frameworks, such as the Goddard finite volume model (Tao et al. 2009), rely upon embedded cloud-resolving models (CRMs) to simulate convective events within and between grid points. Differing from a CRM concerned with local convective initiation (i.e., cold pools and surface fluxes), a CRM employing an ensemble approach, such as that used in the Goddard Cumulus Ensemble (GCE) model (Tao and Simpson 1993; Tao et al. 2003), allows the development of clouds of various life cycle stages and sizes at multiple vertical levels. This is accomplished by representing convection as a statistical occurrence of cloud and precipitation properties. These CRMs may also be used in a stand-alone respect to study specific events [see Tao (2007) for an overview of CRMs and their uses]. Previous research in West Africa has focused primarily on large-scale

features and precipitation. Case studies have been undertaken to illuminate mesoscale and synoptic processes (e.g., Penide et al. 2010; Schwendike and Jones 2010), though little work has been done to explore the degree to which convective characteristics are represented in CRMs in West Africa. It is unclear if convective events produced by CRMs embedded in GCMs accurately represent differences observed in convective characteristics during the WAM season.

The grid spacing employed here corresponds to state-of-the-art GCMs that are now utilizing grid spacings down to 1 km. This scale remains important to allow further study of multiscale interactions, which is especially important to the WAM system. This study explores the statistical representation of explicitly simulated convection from a CRM used by the Goddard finite volume GCM system compared to ground-based radar observations. Two distinct events during the 2006 WAM in the Sahel region are simulated using the GCE model: one associated with an AEW trough (8 September 2006) and another with no AEW influence (14 July 2006). The peak of the monsoon occurs in August in the Sahel and the cases occur during the beginning (14 July) and end (8 September) of the 2006 monsoon season. A discussion of the performance of the CRM microphysical and parameterization packages as applied to intense, tropical convection is provided. This study establishes the model performance of the GCE following recent updates in parameterization schemes that improve ice microphysics representations.

2. Methodology

a. Simulation setup

The CRM used to simulate MCSs that occurred when an AEW was present (8 September 2006) and when no AEW was present (14 July 2006) in this study was a 3D version of the GCE model. The model setup was extensively described in Zeng et al. (2009), with an ice enhancement parameterization (Zeng et al. 2011) included to increase ice crystal concentrations to better represent West African MCSs (Powell et al. 2011; Tao et al. 2011). Briefly, the equations used were non-hydrostatic and anelastic. The GCE accounted for both solar radiation absorption and scattering, and infrared radiation emission and absorption. Turbulent processes (subgrid scale) were parameterized based upon the Klemp and Wilhelmson (1978) and Soong and Ogura (1980) schemes, with both moist and dry processes used in the generation of subgrid-scale kinetic energy. Surface fluxes were provided by large-scale forcing calculations, discussed below and in section 2b.

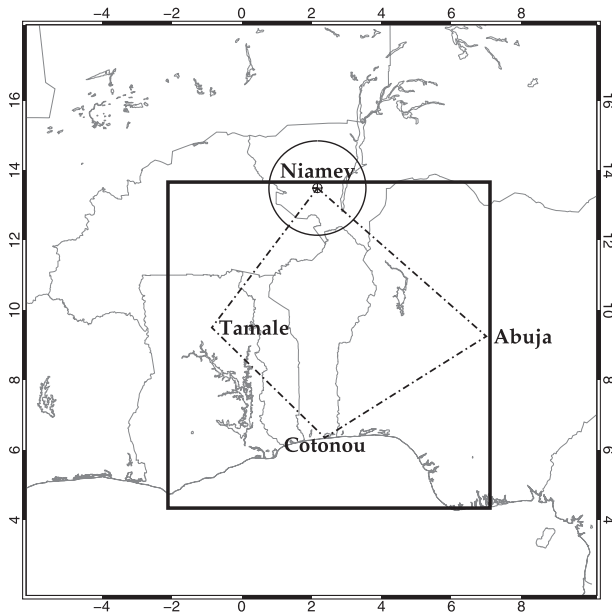


FIG. 1. Map of the simulated region (solid-lined box) in West Africa. The sounding domain (dashed-dotted lines) used to calculate the large-scale forcing data for the simulations is shown, with radiosonde sites labeled. The circle indicates the 150-km-radius MIT ground radar-observed domain.

A one-moment, three-category ice (cloud ice, snow, graupel) scheme (Rutledge and Hobbs 1984) with modified cloud microphysics (Lang et al. 2007; Zeng et al. 2008) along with two water categories (cloud and rainwater) was used. Prognostic hydrometeor variables (expressed as mixing ratios) were produced for each category. Cloud ice and snow were represented by small ($<50 \mu\text{m}$) and large ($\geq 50 \mu\text{m}$) diameter crystals. Different densities were used for graupel (0.4 g cm^{-3}) and snow (0.1 g cm^{-3}). Convective and stratiform partitioning was performed using the GCE method described in Lang et al. (2003), which showed that resultant reflectivity statistics were comparable to statistics created from various simulation and observational partitioning techniques.

Simulations were performed using $1024 \times 1024 \times 63$ grid points with 1-km horizontal spacing and stretched vertical spacing ranging from 42.5 m near the surface to 1 km at the top. Large-scale forcing was employed to drive simulations, provided by a quadrilateral rawinsonde network that was part of the African Monsoon Multidisciplinary Analyses (AMMA; Redelsperger et al. 2006; Lebel et al. 2010) field campaign (see Fig. 1 for simulation domain). To ensure that the large-scale forcing was responsible for heat, moisture, and momentum within the simulation domain, cyclic boundary conditions were used. The domain size was chosen to encompass the forcing network data and provide a large enough area to represent the MCSs. Simulation vertical data were

degraded to 1-km spacing to match observational data (discussed in next section).

b. Observational data

Reflectivity and Doppler velocity data were collected with the C-band, single-polarization Massachusetts Institute of Technology (MIT) Doppler radar and vertically pointing W-band Atmospheric Radiation Measurement (ARM) program Cloud Radar (WACR; Miller and Slingo 2007; Slingo et al. 2008) located in Niamey, Niger (13.49°N , 2.17°E), during the 2006 AMMA experiment. The MIT radar was operated from 5 July to 27 September acquiring both 360° volume plan position indicator (PPI) and range-height indicator (RHI) scans (when convection was present) during a 10-min repeat cycle [see Guy et al. (2011) for further details]. The WACR was operated throughout the AMMA experiment, acquiring semicontinuous observations with $\sim 45\text{-m}$ vertical and 2.5-s temporal sampling. Detectable signal thresholding as a function of height was applied as in Penide et al. (2010). While WACR observations for the 8 September case covered the entire observed time period of the system near Niamey, only the forward anvil was sampled during the 14 July case. Cloud radar data were degraded to 1-km spacing to match the MIT radar Cartesian grid data discussed below.

Scanning radar polar coordinate data were interpolated to a 1-km vertical and horizontal resolution Cartesian grid using the National Center for Atmospheric Research REORDER software (Mohr et al. 1986), corresponding to the GCE simulation output horizontal grid spacing. Radar reflectivity Z volume scans were partitioned into convective and stratiform components using the Steiner et al. (1995) algorithm, which uses a convective threshold value to identify convective cores, along with a convective peakedness criterion that evaluates the surrounding pixels for convective classification. Further details regarding MIT radar data and processing can be found in Guy et al. (2011).

Ground-based radar observations were used as the primary data source for comparison to GCE simulations. Rainfall R estimates were obtained using separate convective and stratiform Z - R power-based relationships from Russell et al. (2010) for each case, where Z is in $\text{mm}^6 \text{ m}^{-3}$ and R in mm h^{-1} . The 8 September case used $Z = 143R^{1.36}$ (convective) and $Z = 256R^{1.22}$ (stratiform), while $Z = 186R^{1.35}$ (convective) and $Z = 299R^{1.46}$ (stratiform) were applied for the 14 July case.

Ice and liquid water mass were calculated using three-dimensional reflectivity data, following a modified methodology of Petersen et al. (2005). Ice water content (IWC; from the -5°C level to echo top) was calculated for each grid point using an exponential size (mass; M)

distribution in the form of an M – Z relationship (Carey and Rutledge 2000):

$$\text{IWC} = 1000\pi\rho_i N_0^{3/7} \left(\frac{5.28 \times 10^{-18}}{720} Z \right)^{4/7} \quad (\text{g m}^{-3}), \quad (1)$$

where IWC is mass per volume, Z is in $\text{mm}^6 \text{m}^{-3}$, N_0 is the constant intercept parameter ($4 \times 10^6 \text{m}^{-4}$), and bulk ice density ρ_i varies between 100 and 800g m^{-3} as a function of Z and precipitation type (stratiform or convective). Similarly, liquid water content (LWC; from near surface to the 0°C level) was calculated using the relationship from Tokay et al. (2002):

$$\text{LWC} = 3.5 \times 10^{-3} Z^{0.536} \quad (\text{g m}^{-3}). \quad (2)$$

Temperature T data from the Niamey sounding site were used to find the 0° and -5°C levels. To approximate the IWC of the associated anvil cloud, WACR radar data were employed using the M – Z – T relationship for 95-GHz observations in the tropics given by Eq. (16) in Protat et al. (2007):

$$\log_{10}(\text{IWC}) = 4.57 \times 10^{-4} Z_{\text{dB}} T + 9.69 \times 10^{-2} Z_{\text{dB}} - 2 \times 10^{-4} T - 0.61 \quad (\text{g m}^{-3}), \quad (3)$$

where Z_{dB} is in decibel units and T is in $^\circ\text{C}$. All IWC and LWC calculations are approximate, as a number of assumptions were used to develop the relationships. Because this study will focus on comparing the relative trends and not absolute magnitudes between simulations and observations, any errors in relationships should not impact study results. Integrating IWC and LWC vertically yields ice water path (IWP) and liquid water path (LWP), respectively.

Hydrometeor identification (HID) is normally derived from dual-polarimetric radar data, which use information from vertically and horizontally polarized signals to estimate hydrometeor species. Some alternative techniques utilizing only horizontal polarization data have been developed. Lerach et al. (2010) developed a method to perform HID analyses using reflectivity and environmental temperature data only. In their study, a HID analysis using a fuzzy logic-based method (Liu and Chandrasekar 2000) was applied to reflectivity observations from an S-band profiler. The methodology was verified using dual-polarization data obtained by the National Center for Atmospheric Research (NCAR) S-polKa radar, which was operating near the profiler. This information was then employed to tune a lookup table method in which HID analysis was a function of only reflectivity and environmental temperature data.

This methodology was applied to MIT radar reflectivity and sounding data to produce a three-dimensional volume HID analysis.

The radar bright band (a layer in which descending aggregates of ice particles begin to melt and form an outer sheath of liquid water, which results in enhanced reflectivity returns due to differences in the dielectric constant between ice and water) can often corrupt HID analysis. In the original methodology of Lerach et al. (2010), vertical velocity measurements were used to detect the brightband layer and consequently removed with a linear interpolation of reflectivity data from above and below the layer. Because the MIT radar was not vertically pointing, Doppler velocity information in the vertical was not directly available and therefore an alternative brightband detection algorithm was employed.

In this study, the following brightband layer detection was used: the 0°C isotherm was found from the nearest environmental sounding for points identified as stratiform by the convective–stratiform separation algorithm. The bright band was assumed to extend below this level by 300 m. The top boundary was identified through analysis of the vertical gradient of reflectivity (Fabry and Zawadzki 1995), which required a decrease between 5 and 10dBZ km^{-1} . Finally, 62.5% of surrounding points (5 of 8 neighboring points in the horizontal) must be identified as stratiform, which helped to alleviate spurious results in the proximity of a convective core, yet not fully exclude smaller brightband regions. Though these brightband-identified regions should be nearly equivalent to the wet snow category, an additional category of melting ice was introduced to indicate the unique identification and determine the performance of the algorithm. Specific temperature and reflectivity criteria can be found in Fig. 4 of Lerach et al. (2010). Categories identified by the algorithm were drizzle (DZ), rain (RN), dry snow (DS), wet snow (WS), dry graupel (DG), wet graupel (WG), hail (H), melting ice (MI), and unclassified (UN; no classification criteria met).

The GCE variables represented instantaneous values at each hour. Radar observations, initially in 10-min time steps, were degraded to 1-hourly temporal resolution to match the GCE data. The closest radar volume time step was chosen, as long as it occurred within 15 min of the GCE time step.

Six-hourly (0000, 0600, 1200, and 1800 UTC) radiosonde data were collected in Niamey during the operational period of the MIT radar. Thermodynamic parameters were calculated using sounding data to characterize the environment before, during, and after the time period of the cases. Pseudoadiabatic parcel ascent from a mixed layer (bottom 50 hPa of sounding) was used in convective available potential energy (CAPE) and convective

TABLE 1. Mean FSS of reflectivity distributions coinciding with observational time period and with model shifted for best agreement. Scores were calculated at each corresponding grid height of MIT radar observations and degraded GCE simulations.

Case	Data points	FSS value with no adjustment	FSS value after optimal time adjustment
8 Sep	All points	0.44	0.47
	Convective	0.38	0.49
	Stratiform	0.56	0.60
14 Jul	All points	0.74	0.73
	Convective	0.77	0.90
	Stratiform	0.73	0.72

inhibition (CIN) calculations. Low-level shear using surface-to-low-level maximum zonal wind was calculated as in Lucas et al. (2000).

The sounding network (Agustí-Panareda et al. 2010) shown in Fig. 1 was used to calculate large-scale forcing, including the aforementioned Niamey station, along with radiosonde sites at Tamale, Ghana (9.50°N, 0.85°E), Cotonou, Benin (6.35°N, 2.38°E), and Abuja, Nigeria (9.25°N, 7.00°E). Domain-averaged large-scale forcing (e.g., zonal, meridional, and vertical motion vectors) and apparent heat source and moisture sink (Johnson and Ciesielski 2000) were computed using the quadrilateral network, though only the large-scale forcing was used in this study.

c. Analysis

Characteristics of the entire model domain were used in the analysis of simulation data. To quantitatively assess simulation performance in comparison to observations, a variation of Brier skill score, named the fractions skill score (FSS), was calculated (Roberts and Lean 2008; May and Lane 2009). Simulation fractions were compared to observed fractions (using reflectivity probability distributions), where the FSS ranged from 0 (no match) to 1 (complete match). Lag analysis of FSS values exhibited better matches when simulations were offset to earlier time periods than observations. As simulations were driven by large-scale forcing, dependence upon synoptic vertical motions strongly influenced the model. Satellite imagery showed that convective initiation occurred westward of and propagated into the model domain. The GCE model used here was not optimized for initiation, but for statistical comparison of convective characteristics. A shift of 4 h was required for the 8 September case, while 6 h was needed for the 14 July case (Table 1).

While some variables were available for both sets of observations and simulations (e.g., reflectivity), analogous variables (e.g., observed IWC and simulated ice hydrometeor mixing ratios) were used to analyze relative trends and distributions between characteristics of

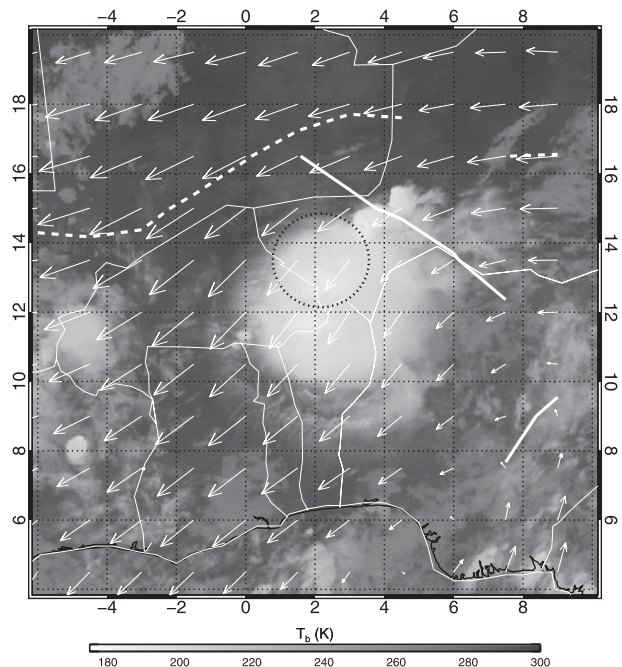


FIG. 2. Observed infrared brightness temperatures at 0600 UTC 8 Sep 2006. Objectively identified AEW trough axis (thick solid line) and AEJ axis (thick dashed line) are shown along with 700-hPa wind vectors (arrows). Wind vectors are proportional to magnitude, with a maximum of 12.6 m s^{-1} and a minimum of 0.8 m s^{-1} . The MIT radar sampling domain is indicated by the dotted black circle.

observations and simulations. The time evolution of observed and simulated characteristics was compared in a total and mean sense. Contoured frequency-by-altitude diagrams (CFADs; Yuter and Houze 1995) were constructed to explore vertical structure and frequency distributions of reflectivity.

Comparison statistics were derived from smaller domains than the model simulations themselves. Given the differences in domain sizes, the magnitudes were not expected to correspond directly. However, because of the large size of the sampled MCSs and the fact that MCSs are a conglomerate of many smaller features (as indicated in section 3), a subsample of the most salient features [squall-line MCSs (SLMCSs), discussed herein] provided a reasonable basis for comparison between radar observations and the GCE model data.

3. Synoptic and mesoscale description

a. 8 September 2006 case

As documented by Penide et al. (2010), a highly organized squall-line MCS [with extensive cloud shield of $\sim 600\text{-km}$ diameter in infrared (IR) imagery] approached Niamey from the southeast and was sampled by the MIT radar at 0200 UTC 8 September. This SLMCS

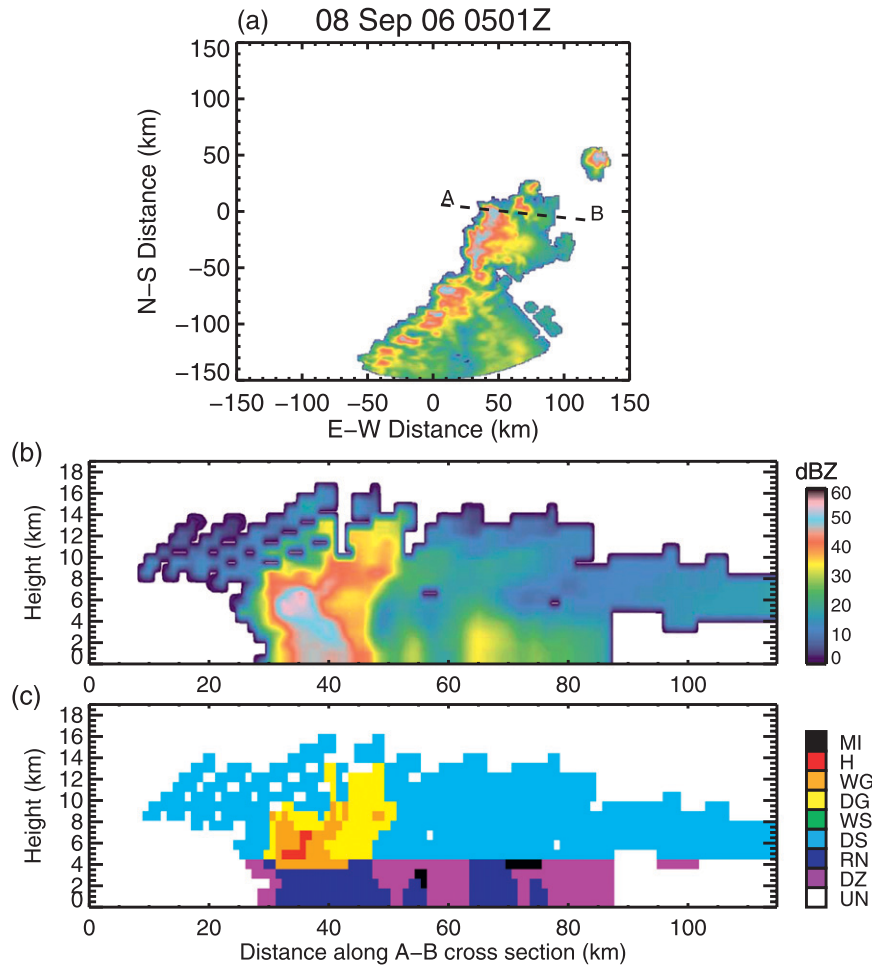


FIG. 3. An example of MIT radar reflectivity (a) 2-km CAPPI at 0501 UTC 8 Sep 2006. Vertical structure of the squall-line MCS is indicated by a cross section of (b) reflectivity, and (c) HID analysis results. Distances in (a) are relative to radar location and the dashed, black A-B line represents cross sections displayed in (b) and (c). Hydrometeors identified in (c): MI, H, WG, DG, WS, DS, RN, DZ, and UN.

was associated with an AEW that was generated near or eastward of 20°E (Janicot et al. 2008; Schwendike and Jones 2010; Zawislak and Zipser 2010) and later was responsible for the genesis of Hurricane Helene in the Atlantic. Analysis of infrared brightness temperature maps over West Africa (not shown) revealed that the associated MCS was generated at 0430 UTC 7 September near 11.5°E and moved westward until dissipating in Burkina Faso (~ 200 km west of Niamey) at approximately 1200 UTC. The African easterly jet (AEJ) was located north of Niamey (Fig. 2), with a northwest-southeast-oriented AEW trough axis (with a speed of 6.5 m s^{-1}) situated to the north and east of the study domain. The SLMCS was ahead or close to within the trough near Niamey, with a northerly component evident in the 700-hPa wind field.

Radar data showed that two distinct convective lines formed the SLMCS, which began to decay near and within the radar domain. The initial convective line observed moved from southeast to northwest with an average speed of 10.5 m s^{-1} and reached the radar location at 0551 UTC where it became quasi stationary for approximately 1 h. A westward-propagating secondary convective line, with a speed of 14.8 m s^{-1} , approached the MIT radar before decaying and becoming less organized. This second surge resulted in the system passing directly over the radar at 0701 UTC and maintaining an estimated average system speed of 13 m s^{-1} while in the observed radar domain. Plan view and vertical cross sections (Fig. 3) clearly showed a leading convective line structure (initial convective line) with prominent front and rear stratiform anvils and the performance of the

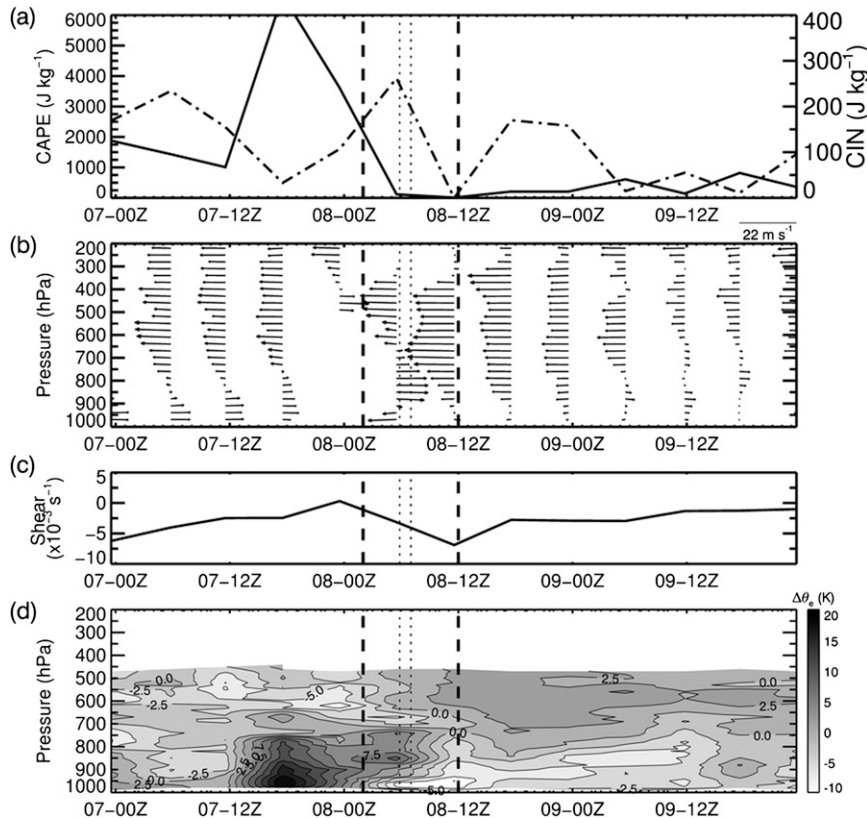


FIG. 4. Time series of (a) CAPE (solid line) and CIN (dashed-dotted line), (b) wind magnitude and direction (toward arrow head), (c) low-level vertical wind shear, and (d) equivalent potential temperature anomaly for the 8 Sep 2006 case. Heavy vertical, dashed lines represent the time period corresponding to ground-based radar observations in Niamey. Thin dotted lines show the times when MCS was directly over the radar. The abscissa axis format is day-UTC time.

HID algorithm. The distribution of HID categories was similar to that shown in Evaristo et al. (2010), which used dual-polarimetric information of a squall line sampled in Benin.

Time series of environmental properties (Fig. 4) revealed that extremely large values of CAPE (Fig. 4a) in excess of 6000 J kg^{-1} at the Niamey sounding site preceded the system, and remained near 3500 J kg^{-1} when the SLMCS entered the radar observational domain (0201 UTC). Westerlies up to 800 hPa were overlaid by deep easterlies until about 1800 UTC 7 September (Fig. 4b), providing moderate low-level vertical wind shear ($2.5 \times 10^{-3} \text{ s}^{-1}$ easterly; Fig. 4c). Figure 4d revealed large positive equivalent potential temperature θ_e anomalies leading up to convection entering the MIT radar domain, consistent with the extreme buildup of CAPE (Parker 2002). A positive anomaly in the 800–500-hPa layer, as well as cold θ_e low-level anomalies following the MCS passage, was indicative of the vertical moisture transport (Scialom and Lemaître 2011) and the downdraft drying and evaporative cooling observed in

this region (Parker et al. 2005), respectively. These characteristics follow the intense convective category of Nicholls and Mohr (2010), except for the shear, which is weaker than reported in their study ($4.4 \times 10^{-3} \text{ s}^{-1}$ easterly; their Table 3).

b. 14 July 2006 case

In contrast to the 8 September case, the 14 July SLMCS was not associated with an AEW event. An AEW trough was located more than 7° west of Niamey, with the AEJ to the south and nearly zonal easterly flow at 700 hPa (Fig. 5). Smaller areal coverage of the system was observed ($\sim 400 \text{ km}$ in diameter via IR imagery) due to a smaller stratiform area. Two distinct westward-propagating MCSs, arriving in the Niamey region simultaneously (0211 UTC), were observed in radar imagery (not shown).

The northern SLMCS (a well-developed bow echo moving westward at a speed of 20 m s^{-1}) was generated near 7°E at 1630 UTC 13 July, while the southern MCS (northwestward movement at 13 m s^{-1}) was generated

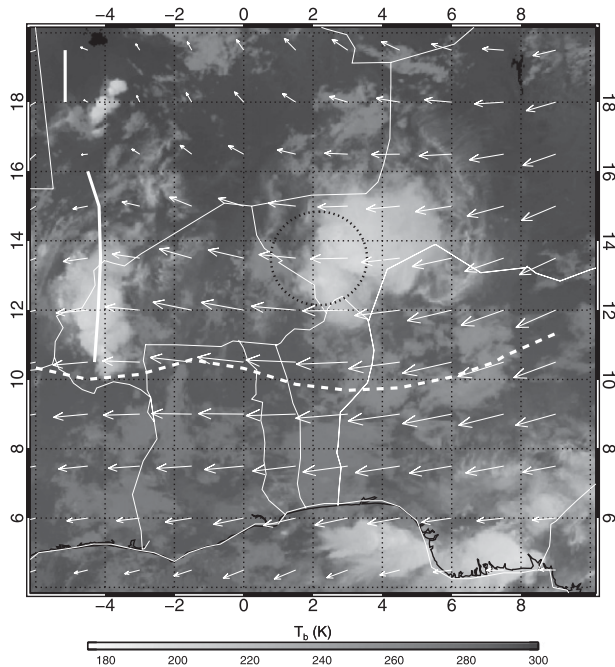


FIG. 5. As in Fig. 2, but for 0500 UTC 14 Jul 2006. Wind vectors are proportional to magnitude, with a maximum of 15.1 m s^{-1} and a minimum of 1.3 m s^{-1} .

near 5°E at 2230 UTC 13 July. The two MCSs merged over the radar location at 0511 UTC, at which time the system began to disorganize and became less linear in nature, moving westward at an average speed of 17 m s^{-1} . Dissipation again occurred in Burkina Faso, apparently generating two new MCSs afterward. The horizontal and vertical structure of the system (as seen in Fig. 6) revealed differences in comparison to the 8 September case. A shorter life span was observed in the radar domain, resulting in different temporal characteristics. This is discussed further in section 4a.

Moderate CAPE ($\sim 1500 \text{ J kg}^{-1}$) and very little CIN ($\sim 100 \text{ J kg}^{-1}$; Fig. 7a) characterized the environment before the arrival of the MCSs. A moist mixed layer ($\sim 15 \text{ g kg}^{-1}$; not shown), along with strong low-level vertical wind shear ($5\text{--}20 \times 10^{-3} \text{ s}^{-1}$ easterly shear; Fig. 7c), provided a favorable environment for organized convection. Bowing curvature of the leading convective line (Fig. 6a) evidenced a strong rear-inflow jet associated with the system.

Analysis of IR imagery loops (not shown) indicated that both systems were in a mature life cycle phase when entering the radar domain, and both systems decayed in the western region of the radar domain. Similar life cycle phase and system morphology allowed direct comparison of the two events, though the size difference (greater horizontal coverage of the 8 September case)

and temporal extents within the radar domain (8 and 11 h for the 14 July and 8 September cases, respectively) should be noted. No dry intrusions (i.e., Saharan air layer) are apparent in either case and both systems are driven by moist low-level environments and strong vertical wind shear.

Guy et al. (2011) showed that precipitation and MCS size are both larger in this region when an AEW is present. Differences in convective (increase) and stratiform (decrease) precipitation during an AEW event indicate that different microphysical properties are likely present, given the coupling of convective lines and trailing stratiform shields (discussed later). Berry (2009) suggested that AEWs may promote the maintenance of convective systems when occurring in and ahead of the trough axis (as in the 8 September case), which could act to increase ice species through convective invigoration and/or maintenance and extension of the trailing stratiform area.

4. Discussion

a. Observations

Time series presented in Fig. 8 indicated the temporal evolution of characteristics of both cases using MIT radar data. The analysis of volumetric rain (Fig. 8a; total rain rates of echo area) indicated the importance of both the convective and stratiform components in both cases. During the 8 September case, precipitation was dominated by the convective component during the first half of observations. During the second half, stratiform precipitation contributed slightly more total rain. Stratiform precipitation contributed less in the 14 July case, where only the last 2 h showed slightly greater precipitation from the stratiform component. The secondary peak noticeable in each case resulted from secondary convective lines previously discussed.

Strong updrafts result in increased lofting of hydrometeors, so consequently the vertical structure of radar reflectivity is useful for studying convective strength. The maximum height of the 30-dBZ echo (30ETH; DeMott and Rutledge 1998) is a common intensity metric. Figure 8b showed higher 30ETH values for the 8 September case, with a peak near 19 km, while only about 15 km for the 14 July case. Heights decreased throughout the observed time periods. The existence of 30ETH well above the environmental freezing level indicates the presence of mixed-phase processes accompanied by significant lightning. Peaks in frequent lightning flashes (not shown) coincided with maximum convective activity (0300 and 0700 UTC 8 September

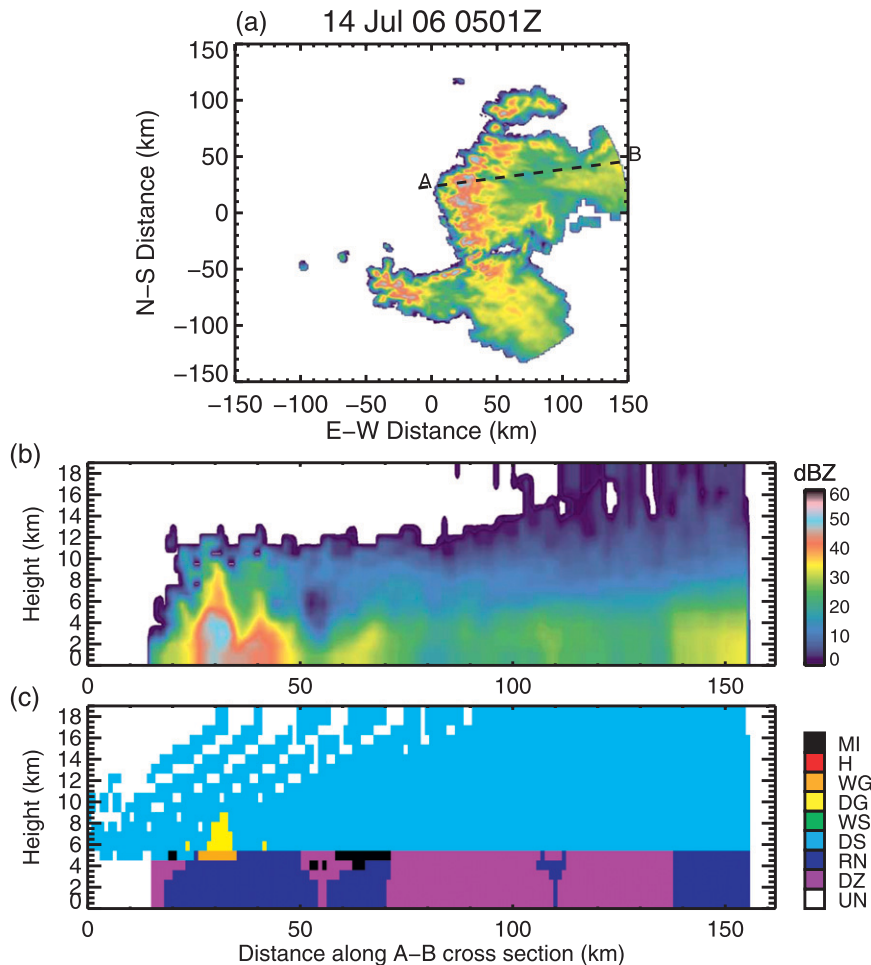


FIG. 6. As in Fig. 3, but for 0501 UTC 14 Jul 2006. Note that some beam filling issues were present at upper levels at distances greater than 100 km.

and 0400 UTC 14 July). Additionally, 0ETHs indicated stratiform shields at high altitudes, with the 14 July case extending to the top of the analysis domain. Lower 30ETHs associated with the second convective portion suggested that updrafts were weaker in the second convective portion than the first, with a likely reduction in mixed-phase particle production (also indicated by a decrease in lightning flashes).

Decreased lofting of hydrometeors also affects ice production, as evidenced by the evolution of IWP (Fig. 8c) and LWP (Fig. 8d). Trends were similar to volumetric rain—not surprising given that both were a function of radar reflectivity (see section 2b). The double peaks of the stratiform IWP and LWP in the 8 September case lagged the convective portion by 1–3 h, with a slight difference in slope. A single peak was observed during the 14 July case. During increased convective periods, ice particle transport occurs from convective cores into the stratiform region. These ice particles then fall out of

the stratiform region, resulting in higher water contents. This was manifested as an increasing separation of the IWP and LWP curves following each convective activity peak.

The analysis of IWC and LWC showed varying vertical structure between the cases, despite similar IWP and LWP magnitude and trends. Time–height plots in Fig. 9a showed increased mean IWC (contoured), followed by increased mean LWC (shaded) for the 8 September case, in agreement with the discussion above. The more vigorous convection associated with the initial convective line was evident in maximum distributions (Fig. 9b). The distributions in Fig. 9 indicated that maximum values did not necessarily follow mean distributions and were dependent upon convective morphology and the intensity of individual features. Mean IWC evolution (Fig. 10a) appeared more homogeneous for the 14 July case, though mean LWC (Fig. 10a) was similar. Contours of high IWC resided

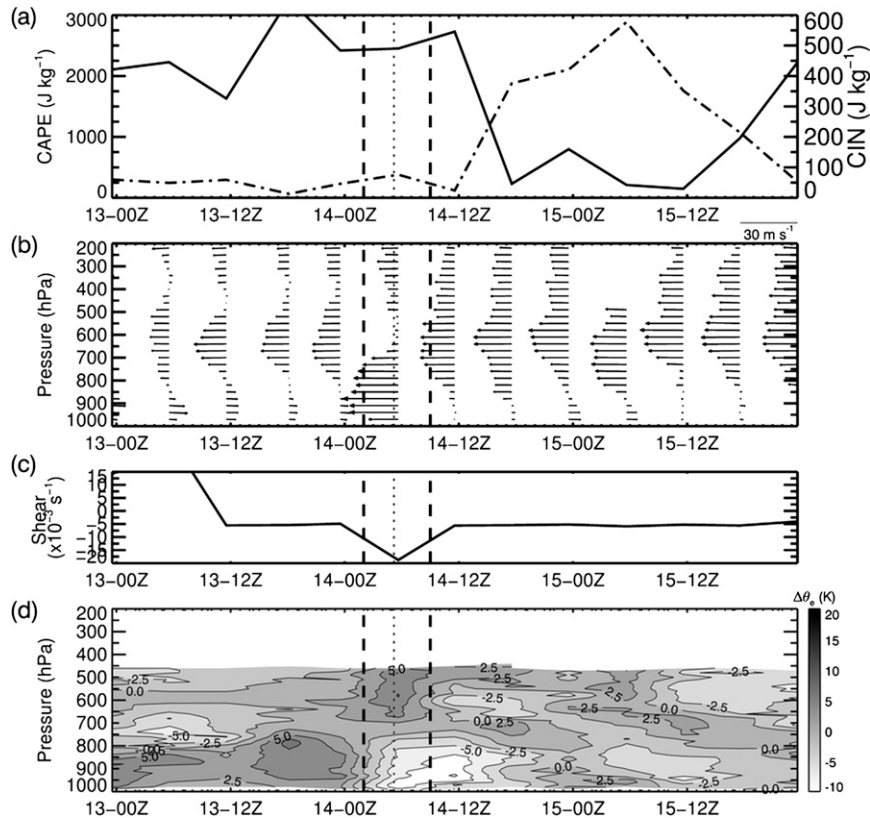


FIG. 7. As in Fig. 4, but for the 14 Jul 2006 case.

at lower heights than the AEW case, while lower-value contours remained at consistent heights, indicating a different distribution of ice mass throughout the entire no-wave MCS case. Time series plots of HID types confirm that graupel distributions were confined to lower altitudes as well as a consistently deeper (and more temporally homogeneous) identification of snow (shown later) in the 14 July case.

The shape of observed CFADs (Figs. 11, 12) exhibited a sharp decrease in reflectivity above the 0°C layer (~4.5 km). Brightband signatures (enhanced reflectivity near the melting level) were also evident in both stratiform distributions (Figs. 11c, 12c), along with a strong evaporative process below the melting level (shown by the large decrease in reflectivity toward the surface). Another utility of CFAD plots is their ability to suggest system morphology and microphysical characteristics of convective events. Greater diagonalization, along with the occurrence of a wider spectrum of reflectivity values during the 14 July case, was indicative of a system with a greater population of cells in the mature phase than the 8 September case. This corroborated temporal observations of the longer-lasting 8 September system. Broader reflectivity distributions aloft for the convective

components (Fig. 11b) of the 8 September case indicated the presence of larger particles aloft (by continued strong convective cores and associated updrafts) compared to the 14 July case (Fig. 12b). The offset of maximum probabilities to lower-reflectivity values in the 14 July case for both convective and stratiform CFADs was at least partly due to a larger population of snow in the upper levels (shown later). Reflectivity values between 35 and 40 dBZ occurred at higher elevations (up to 15 km) compared to the 14 July case (below 8 km), suggesting that a larger graupel population was present.

To provide further analysis, height-probability frequencies were plotted for HID species (Fig. 13) identified using the algorithm described in section 2b. In agreement with the above analysis, 14 July showed a greater snow occurrence at upper levels, though all other ice species (except dry graupel) occurred with higher frequency above 7 km during the 8 September case. Both wet and dry graupel and hail distributions extended farther aloft during the 8 September case, contributing to the higher occurrence of reflectivity values aloft noted earlier. Extensive brightband occurrence (melting ice) was present in both cases.

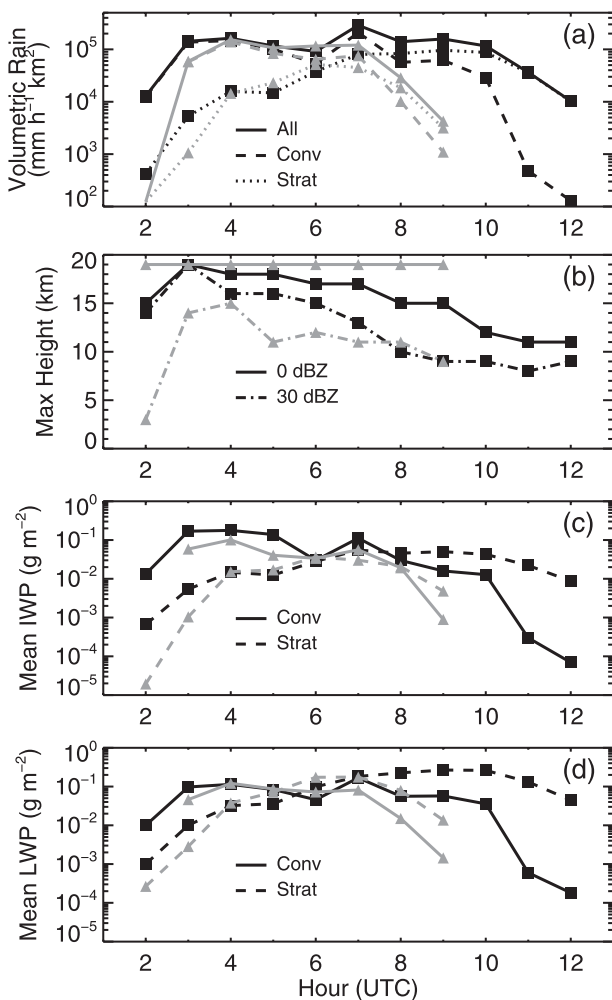


FIG. 8. Time series of the (a) total (solid line), convective (dashed line), and stratiform (dotted line) volumetric rain, (b) maximum height of 0 and 30 dBZ (solid and dashed lines, respectively), and mean (c) IWP and (d) LWP fractions for convective (solid line) and stratiform (dashed line) regions derived using MIT radar data from 8 Sep (black with squares) and 14 Jul (gray with triangles) 2006. Note that (a) and (c),(d) are displayed with logarithmic ordinate axes.

b. Simulations

Probability distributions of rain rate (Fig. 14) showed too large a population of rain rates over 10 mm h^{-1} and too few small rain rates. Total precipitation was a function of lower stratiform and higher convective rain rates compared to observations (not shown). As such, the distributions indicate that the 8 September case produced a larger convective precipitation deviation from observations. Though convective and stratiform fractions were comparable to observations, there was a larger occurrence of high reflectivities, which acted to shift the probability distribution in the aforementioned manner.

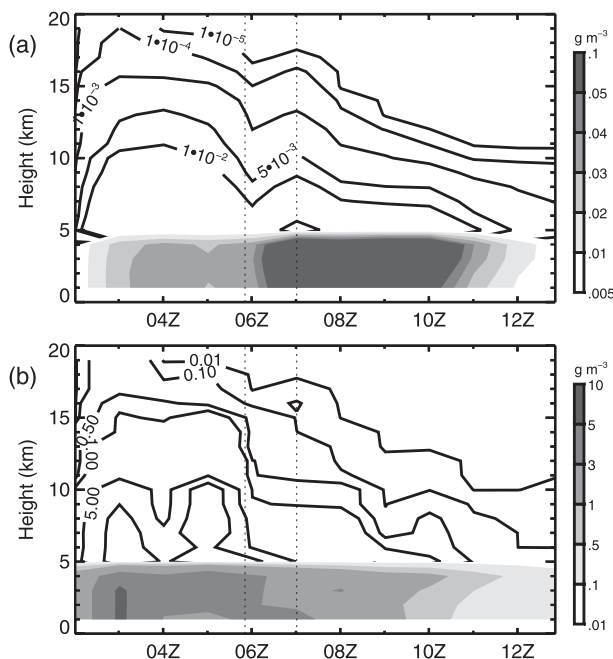


FIG. 9. (a) Mean and (b) maximum radar-derived water content during the 8 Sep 2006 case. IWC is open-contoured with intervals of 0.000 01, 0.0001, 0.001, 0.005, and 0.01 in (a) and 0.01, 0.1, 0.5, 1.0, 5.0, and 10.0 in (b), while shading corresponds to LWC in both. Thin vertical dotted lines show the approximate time of passage of the system over the radar.

Time series of maximum reflectivity values (Fig. 15) indicated this behavior, with high reflectivity values persisting at low levels within the simulations for a longer time period than observed. This behavior is consistent with previous studies using the GCE model and suggested that convective decay occurred more slowly in simulations. High reflectivity values ($>50 \text{ dBZ}$) were limited to heights near and below the freezing level in the model, similar to Lang et al. (2011). Cases analyzed here were more intense (e.g., higher reflectivity aloft) and larger than those considered in Lang et al. (2011) and displayed a larger relative graupel signature aloft (discussed later). Moderate to high reflectivity values (20–50 dBZ) were well represented, though more persistent and less variable (especially vertically) than in observations. Observed echo-top heights were higher than simulated, a common occurrence with this model (S. Lang 2011, personal communication), though changes in echo-top height were found. While only results for 8 September are shown, the 14 July case displayed similar characteristics.

Simulated CFADs (Figs. 11, 12) exhibited modal values between 0 and 5 dBZ in the total and stratiform distributions and similarly broad distributions throughout each (total, convective, and stratiform) portion.

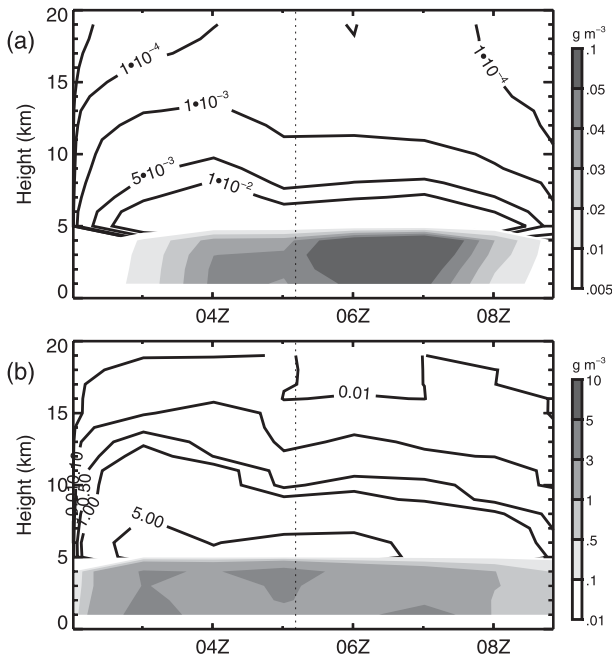


FIG. 10. As in Fig. 9, but for 14 Jul 2006.

However, the 8 September case was offset to higher reflectivity values throughout the vertical plane. Diagonalization was present in convective distributions, but not, however, represented in stratiform and therefore total distributions. The high occurrence of large

reflectivity values (Fig. 15) acted to offset the distributions toward larger values and decrease the diagonalization. A brightband signature was present in the stratiform distribution near 3–4 km, along with a higher frequency of larger reflectivity values aloft.

Bryan and Morrison (2012) showed that squall-line systems were extremely sensitive to horizontal grid size. A decrease in horizontal grid spacing from 1 km to 250 m resulted in a decrease of 10%–30% in total precipitation. In discussing the differences between precipitation and reflectivity distributions, the ice microphysics scheme (single moment) employed in this study should also be considered. Two-moment schemes (which predict not only mixing ratios for hydrometeors, but number concentrations) have been shown to better represent precipitation (Bryan and Morrison 2012). Additionally, Morrison et al. (2009) showed that two-moment schemes increase reflectivity in the stratiform region as a result of decreased evaporation. It is also likely that large reflectivity values (>50 dBZ) were confined to below 5 km because of the use of graupel in the simulations presented. Figure 3 indicated the presence of hail up to at least 9 km. Despite the system structure differences, the simulations provided a successful forecast of important relative properties of each case following the temporal adjustments applied from the analysis of FSS values.

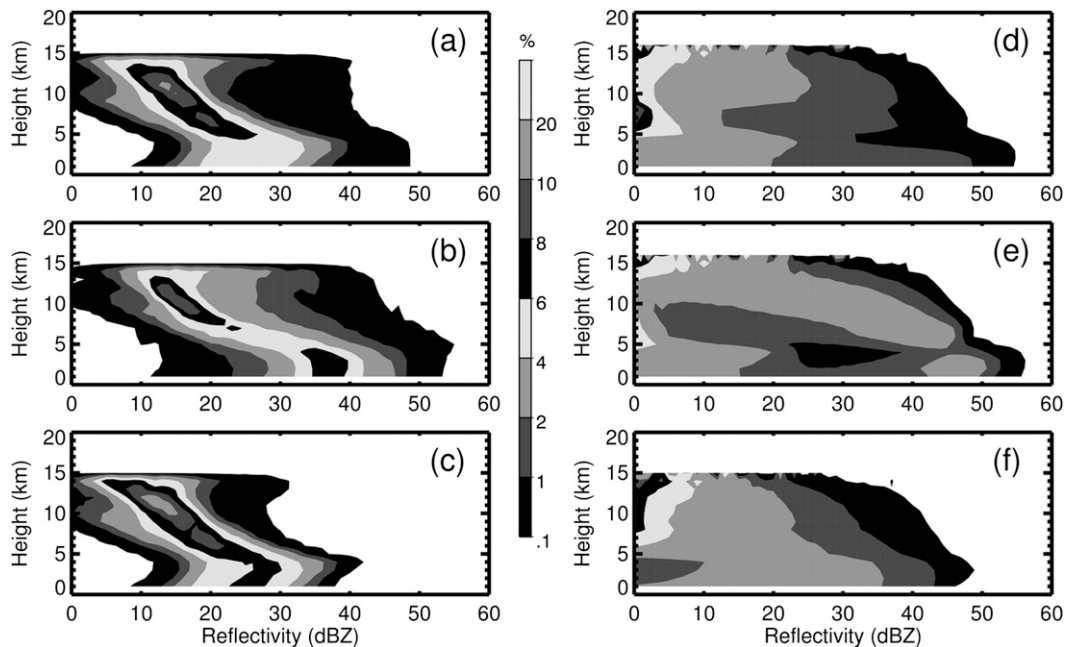


FIG. 11. CFADs of reflectivity for (a)–(c) MIT radar observations and (d)–(f) GCE simulations for the 8 Sep 2006 case using (a),(d) convective, (b),(e) stratiform, and (c),(f) classified data. Shaded contour values for all plots are indicated in colorbar, with units of percentage at each vertical level.

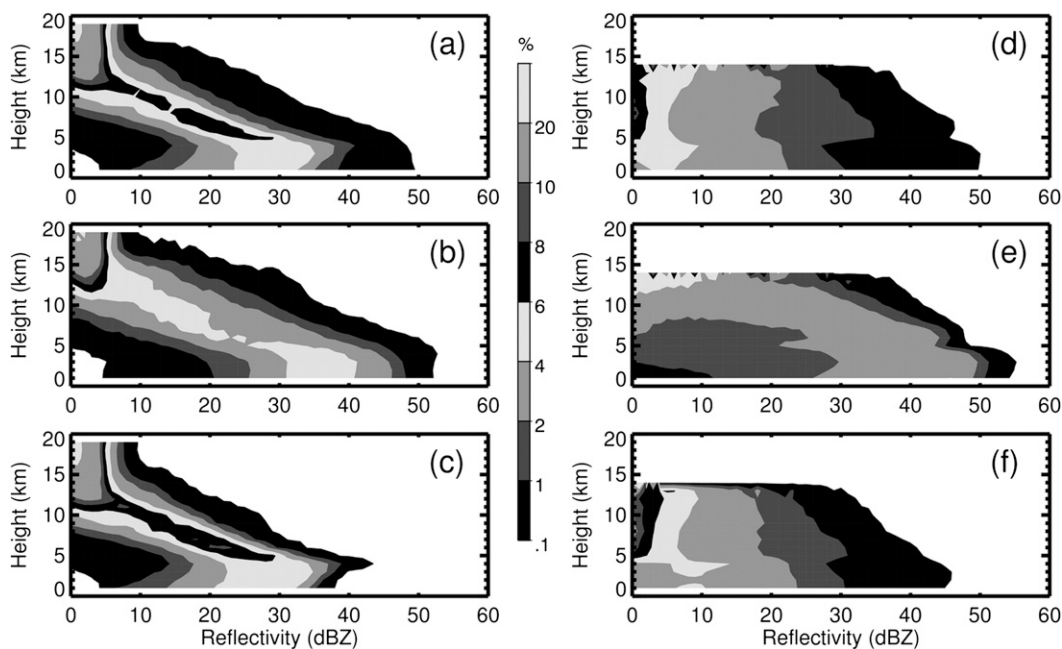


FIG. 12. As in Fig. 11, but for the 14 Jul 2006 case.

c. Observation–simulation comparisons

The most noticeable difference between observations and simulation CFAD reflectivity distributions is the displacement toward lower reflectivity values in the simulations. The simulated modal value between 0 and 5 dBZ was below the sensitivity of the C-band radar observations. Cloud radar data (which have greater sensitivity) were not included in the CFAD distributions because of the lack of observations preceding the 14 July case. As mentioned previously, the use of a single-moment microphysics scheme using graupel as the dense ice species is the likely cause of this discrepancy. A broader distribution was evident for both simulated cases compared to observations (Figs. 11, 12), especially at low levels. Simulated convective components (Figs. 11e, 12e) produced comparable maxima near the surface and diagonalization (decreasing reflectivity with increasing height) as observed (Figs. 11b, 12b). The stratiform component of the 8 September case (Fig. 11c) captured the low-level (below 4 km) evaporative signature.

The vertical distribution of different hydrometeors (section 4a) resulted in unique ice and liquid water mass distributions for each case. Using IWC and LWC calculations, observed vertical distributions may be compared to simulations by way of hydrometeor mixing ratios produced in the model (Fig. 16). These variables are compared because they are both measures of mass,

where IWC and LWC represent ice and liquid water, respectively, per unit volume and the mixing ratio is defined as the mass of the hydrometeor (snow, graupel, and rain in this case) to the mass of dry air. The advantage of using mixing ratios within a model framework is that it presents a way to track conservative and nonconservative water processes. Modeled cloud water distributions have no observational counterpart for comparison since C-band radar is insensitive to droplet size, comparable to cloud droplets in this model. Simulated graupel can be compared with MIT radar-derived IWC, while simulated snow was compared to IWCs derived from both MIT and WACR data. The cloud radar data sampled both leading anvil and trailing stratiform portions of the convective systems (only leading anvil in the 14 July case) and only reflectivity values up to 10 dBZ were retained. This corresponds to the detection of small drizzle droplets, snow, and cloud ice. Therefore, there is some overlap when comparing observed IWCs and simulated mixing ratios.

Liquid water corresponded in both distribution and position, located mostly below the melting level (~ 4.5 km). Simulated graupel for the 8 September case (Fig. 16a) exhibited a slower decrease with height than observations, suggesting that too much graupel aloft was produced. Observed IWCs derived from WACR exhibited a bimodal peak, a result of the leading anvil occurring at higher altitudes followed by the trailing stratiform region (Cetrone and Houze 2011). Simulated

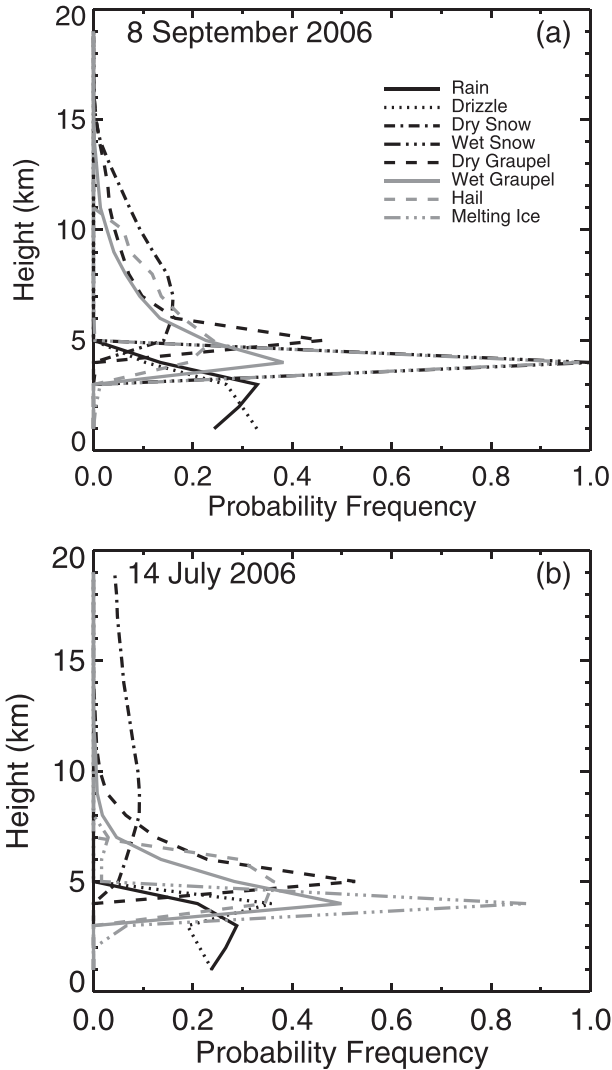


FIG. 13. Occurrence frequency–height distributions of identified hydrometeor types using MIT radar reflectivity and temperature profiles for (a) 8 Sep and (b) 14 Jul 2006 cases. Eight hydrometeor types were identified: rain (solid black line), drizzle (dotted black line), dry (dashed–dotted black line) and wet (dashed–dotted–dotted black line) snow, dry (dashed black line) and wet (solid gray line) graupel, hail (dashed gray line), and melting ice (bright band; dashed–dotted–dotted gray line). Frequencies were calculated as the number of occurrences for each HID species at each vertical level divided by the total number for that species over the column.

ice and possibly a small component of rain distributions agreed well with the lower peak, which stretched from near 5 to 10 km. Modeled cloud ice was offset to a lower elevation than observations suggested. Reduced echo-top heights were noted in the simulations that would directly affect the height of the cloud ice distribution.

Distributions during the 14 July case (Fig. 16b) were somewhat different. Rain was well represented, and graupel distributions corresponded more closely to MIT

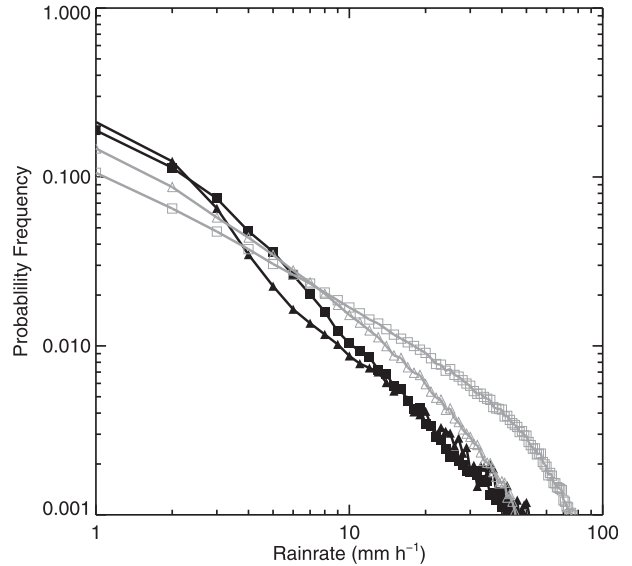


FIG. 14. Frequency of occurrence of rain rates estimated by the MIT radar (black lines) and simulated by the GCE model (gray lines) for 8 Sep (squares) and 14 Jul (triangles) 2006.

radar–derived IWC shape. Simulated snow and cloud ice exhibited a stronger bimodal distribution, but unfortunately, because only the forward anvil was sampled for this case, observations showed only a distribution aloft. Simulated ice hydrometeors were confined to lower elevations and did not extend to upper levels as seen in observations, suggesting that ice transport to upper levels was not well represented for this case.

Differences observed in the mean vertical distributions of ice and water mass revealed strengths and weaknesses of the simulations in comparison to observations. It was of interest to analyze the temporal evolution of these variables to determine how well the observed morphology of the systems was represented by the simulations. A frequency of occurrence by height was obtained by combining dry and wet snow, dry and wet graupel, and rain and drizzle into three categories (snow, graupel, and rain categories, respectively) at each time step. The vertical probability of occurrence for each category was calculated. Corresponding simulated mixing ratios were overlaid on the observed probabilities (Fig. 17). Simulations for the 14 July case produced more realistic hydrometeor distributions over the time period shown, while 8 September simulations resulted in distributions that ended more abruptly than observed (except for snow).

Simulated rain for the 14 July case was similar to observations, while the 8 September simulation appeared to place the majority of rainwater early in the time period with tightly contoured lines. Observations also exhibited a later and broader distribution of liquid

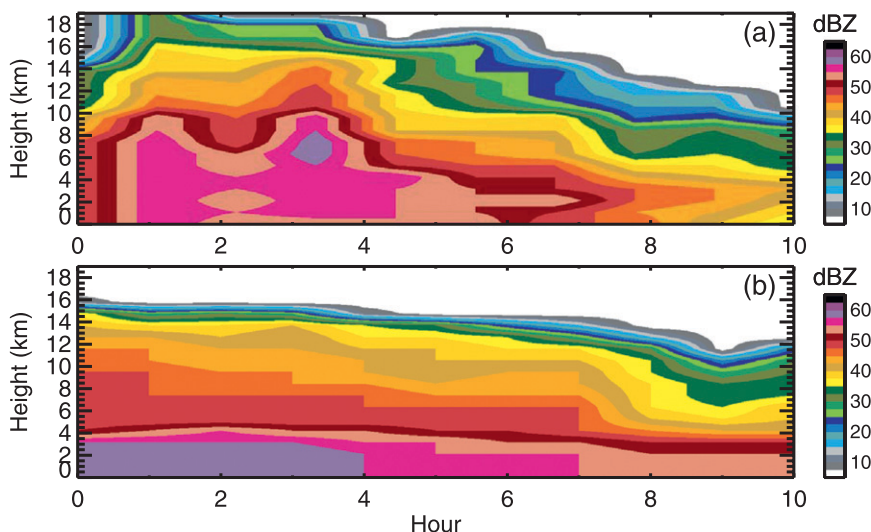


FIG. 15. Time evolution of maximum reflectivity values from (a) MIT radar observations and (b) GCE simulations for 8 Sep 2006. The abscissa corresponds to observed time in the radar domain in (a) and corresponding simulated time period in (b).

water. Simulated graupel occurred at lower elevations than indicated by observations during both simulations. Despite the quickly diminishing simulated graupel during the 8 September period, snow, graupel, and rainwater maxima and evolution were temporally coincident (after the initial time adjustment) for both cases. Simulated snow was better represented during the 8 September case than the 14 July period. In general, the deep vertical extent of the 14 July case was not represented in the model. As mentioned previously, simulations were driven by large-scale forcing, where dependence upon synoptic vertical motion strongly influenced the model. In both cases, there was deep subsidence present between 850 and 450 hPa, indicative of an environment with decaying deep convection present. Synoptic subsidence became quite strong midway through the 8 September case, which led to the abrupt decline in hydrometeor mixing ratios discussed previously. Simulations used linearly interpolated large-scale forcing solutions every hour from each sounding time step (6-hourly). The model was allowed to propagate solutions; no nudging was used to ensure convection matched observations. Therefore, simulations were limited by environmental characteristics associated with mature and decaying convection because of the more eastward position of the sounding network.

5. Summary and conclusions

The 3D Goddard Cumulus Ensemble, a CRM, was used to simulate two West African MCSs during the 2006 WAM season. Model performance was explored

through comparison with ground-based radar data obtained during the AMMA field campaign. The 8 September case was associated with an AEW trough that later went on to generate Hurricane Helene, while the 14 July case showed no association with AEW synoptic forcing. Guy et al. (2011) showed that MCSs associated with AEWs in this region displayed larger stratiform areas and enhanced convective characteristics (e.g., 30-dBZ echo heights) using ground-based radar data over a limited time period during the same season. The analysis of 13 yr of TRMM satellite data indicated similar vertical structures of reflectivity and other convective intensity characteristics, though the stratiform area (fraction) was larger (smaller) for AEW-associated systems (Guy and Rutledge 2012). The cases chosen for this study were generally indicative of this behavior.

Simulations produced convective systems an average of 5 h sooner as compared to the observations. Overall system size was underestimated in each case, though the 8 September case was larger than the 14 July case, as observed in IR imagery. Reflectivity probability distributions were used to calculate FSS values that indicated that simulations exhibited skill in reproducing the convective structure (relative distribution differences between cases and diagonalization) of each case, though stratiform portions were not represented as well (little diagonalization and distributions were too broad throughout). Time series showed that high reflectivity values were present at low levels longer than observed. Despite the abundance of high reflectivity values, observations showed extremely high reflectivity values (>50 dBZ) reaching higher

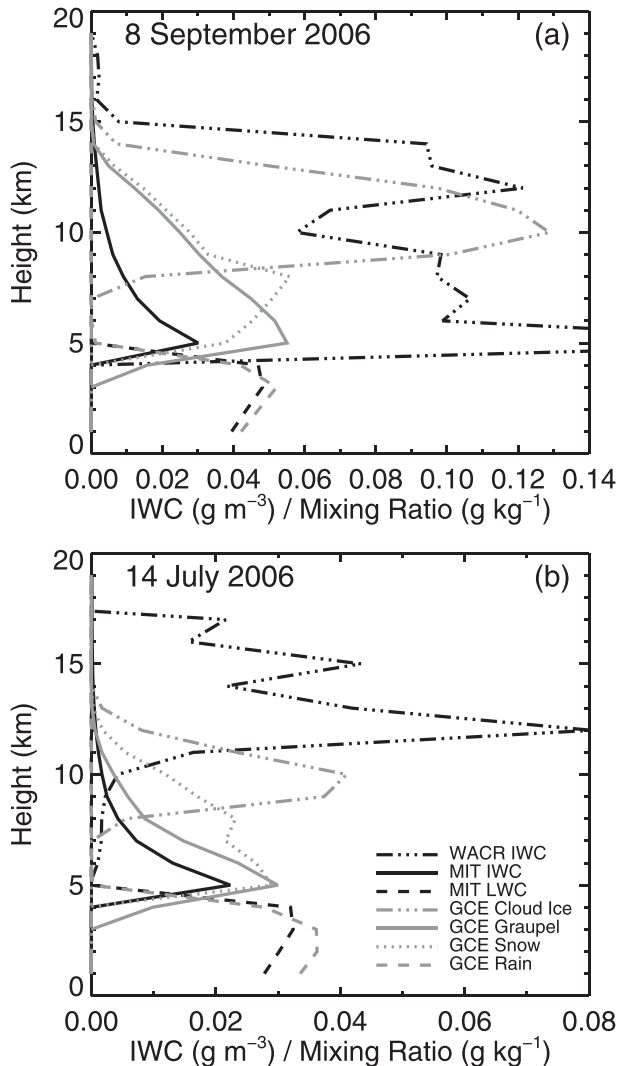


FIG. 16. Mean observed LWC (dashed black line) and IWC (solid and dashed–dotted–dotted–dotted black line) calculated using MIT radar and WACR data, respectively, and simulated rain (dashed gray line), snow (dotted gray line), graupel (solid gray line), and cloud ice (dashed–dotted–dotted–dotted gray line) mixing ratios during (a) 8 Sep and (b) 14 Jul 2006 cases.

elevations (10 km) than simulations (5 km). Simulated bulk precipitation also showed an overestimation (underestimation) of the occurrence of high (low) rain rates. These results are not surprising given the use of a single-moment microphysics scheme.

It should be noted that larger (smaller) CAPE and weaker (stronger) vertical wind shear during the 8 September (14 July) case likely played a role in both the observed and simulated differences discussed in this study. The 8 September case revealed much larger IWC aloft than the 14 July case, despite the fact that the 14 July system exhibited higher observed echo-top heights. This corroborates findings of increased convective

activity (Guy et al. 2011) and convective maintenance (Berry 2009) associated with an AEW event. Mean ice mass in midlevels (especially directly above the melting level) was slightly larger for the 14 July case. Vertical profiles of ice and liquid water indicated that simulations captured the mean distribution of the liquid water mass. The 14 July simulations exhibited a reasonable vertical representation of ice mass, while graupel mass decreased more slowly above the 7-km level than observations during the 8 September simulations. In both cases, the lower vertical extent in the simulations negatively affected the agreement between simulated cloud ice and IWC derived from cloud radar. Cloud ice appeared at lower elevations for both simulations, with a narrower distribution.

Key features of CFAD distributions for each case were reproduced in simulations, such as stratiform brightband and low-level evaporative signature and diagonalization of convective distributions. Broader distributions of the CFADs were found in the simulations, and were especially evident in the convective profiles. Higher frequencies in simulated distributions were offset to lower reflectivity values. In the 8 September case, this appeared to be due to an underestimation of graupel in midlevels, contradictory to the mean profile results. Observed hydrometeor types were identified using a reflectivity and temperature profile algorithm to create a three-dimensional volume estimate. The vertical probability of each category indicated that while the 14 July case exhibited a higher overall probability of graupel, the distribution was confined to lower elevations than the 8 September case. A time series plot of the occurrence of select HID categories overlaid by analogous simulated hydrometeor mixing ratios confirmed that while the timing of graupel (and snow) was generally correct, it was located at lower heights, which affected the vertical distribution of ice mass.

Characteristics of the GCE simulations generally agreed well with observations and reproduced the unique aspects of the two distinct MCSs favorably, with a few caveats. Deviations in vertical ice mass distribution existed between observations and simulations. While the microphysics scheme could contribute to these differences, it was also likely that the representation of the dynamics of the MCSs contributed to the deviation, as storm dynamics are closely tied to microphysics. In addition, misrepresentation due to microphysics may act to modify system dynamics in the modeling framework.

Observed MCS initiation occurred outside the simulated domain and propagated into the study area. Large-scale forcing derived from a sounding network showed that the large-scale environment, while supportive of deep convection, was not optimal. This resulted in a less

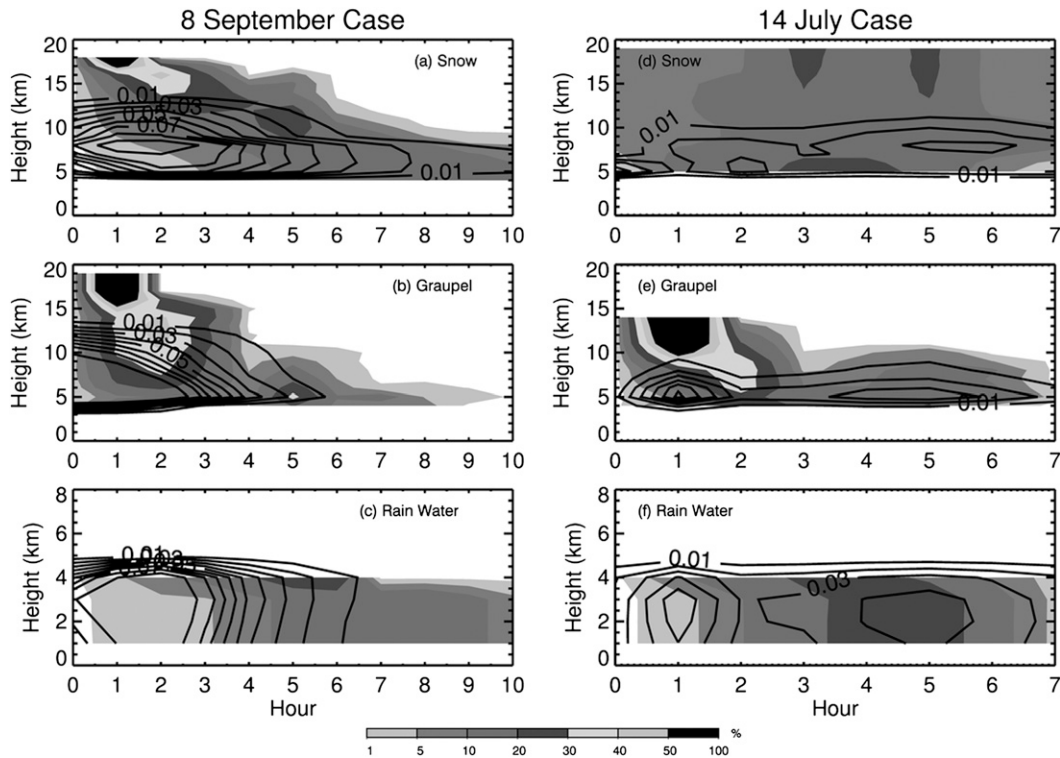


FIG. 17. Time evolution of hydrometeors during the (left) 8 Sep and (right) 14 Jul 2006 cases. Shading denotes probability frequency as a function of height for hydrometeors identified using MIT reflectivity and temperature profiles. Snow and graupel include both wet and dry identified components, while rain includes rain and drizzle hydrometeors. Overlaid are mixing ratios of corresponding hydrometeors with a contour interval of 0.01 g kg^{-1} .

extensive system, which could affect the distribution of microphysical variables. Previous studies have found that reducing the grid size often results in a better representation of the microphysical character of convective systems (e.g., Lang et al. 2007; Bryan and Morrison 2012). Microphysics within MCSs can be complex and variable on small spatial scales, therefore decreased grid size can help to resolve some of these features.

Future work should look at the representation of these (or similar) MCSs with a GCM using an embedded CRM with a longer simulation time. Better representation of system initiation would help to explain the contribution of dynamics to the microphysical differences observed in this study. The bulk of previous work has focused on maritime systems. The analysis of a greater number of tropical continental cases would also help to find biases contributed by differences in kinematic (e.g., updraft and downdraft strengths) and therefore microphysical structure between continental and maritime convection. The use of a two-moment microphysical scheme would likely provide improvement in precipitation and reflectivity distributions. The HID analysis indicated hail within the Sahelian MCS, therefore using hail as the dense ice species in these

tropical continental system simulations may provide a better representation of reflectivity and have an effect on precipitation processes. However, the computational expense should be considered with these additions. Also, synoptic and mesoscale environmental characteristics display both interseasonal and intraseasonal variability. Simulations may provide an ideal environment to explore monthly or seasonal variability between MCSs occurring during both AEW and non-AEW events.

Acknowledgments. This research was supported by the NASA CEAS Fellowship Grant NNX08AT77G and NASA Precipitation Measurement Mission under Grant NNX10AG88G. W.-K. Tao is mainly supported by the NASA Precipitation Measurement Mission (PMM) and NASA Modeling Analysis Prediction (MAP). Based on a French initiative, AMMA was built by an international scientific group and is currently funded by a large number of agencies, especially from France, the United Kingdom, the United States, and Africa. It has been the beneficiary of a major financial contribution from the European Community's Sixth Framework Research Programme. Detailed information on scientific coordination and funding is available on the AMMA International website

(<http://www.amma-international.org>). MIT radar data were provided by Earle Williams. Sounding data were provided by Doug Parker. Cloud radar data were obtained from the Atmospheric Radiation Measurement Program (ARM) sponsored by the U.S. Department of Energy, Office of Science, Office of Biological and Environmental Research, Climate and Environmental Sciences Division. Large-scale forcing data were provided by Paul Ciesielski. Gareth Berry provided computer code for AEW analysis. The authors thank Sue van den Heever for helpful comments on early versions of this work and three anonymous reviewers for comments and suggestions that greatly improved this manuscript.

REFERENCES

- Agustí-Panareda, A., A. Beljaars, C. Cardinali, I. Genkova, and C. Thorncroft, 2010: Impacts of assimilating AMMA soundings on ECMWF analyses and forecasts. *Wea. Forecasting*, **25**, 1142–1160.
- Barthe, C., N. Asencio, J.-P. Lafore, M. Chong, B. Campistron, and F. Cazenave, 2010: Multi-scale analysis of the 25–27 July 2006 convective period over Niamey: Comparison between Doppler radar observations and simulations. *Quart. J. Roy. Meteor. Soc.*, **136**, 190–208, doi:10.1002/qj.539.
- Berry, G. J., 2009: African easterly waves and convection. Ph.D. dissertation, University at Albany, State University of New York, 209 pp.
- Bolton, D., 1984: Generation and propagation of African squall lines. *Quart. J. Roy. Meteor. Soc.*, **110**, 695–721, doi:10.1002/qj.49711046509.
- Bryan, G. H., and H. Morrison, 2012: Sensitivity of a simulated squall line to horizontal resolution and parameterization of microphysics. *Mon. Wea. Rev.*, **140**, 202–225.
- Carey, L. D., and S. A. Rutledge, 2000: The relationship between precipitation and lightning in tropical island convection: A C-band polarimetric radar study. *Mon. Wea. Rev.*, **128**, 2687–2710.
- Cetrone, J., and R. A. Houze Jr., 2011: Leading and trailing anvil clouds of West African squall lines. *J. Atmos. Sci.*, **68**, 1114–1123.
- D'Amato, N., and T. Lebel, 1998: On the characteristics of the rainfall events in the Sahel with a view to the analysis of climatic variability. *Int. J. Climatol.*, **18**, 955–974.
- DeMott, C. A., and S. A. Rutledge, 1998: The vertical structure of TOGA COARE convection. Part I: Radar echo distributions. *J. Atmos. Sci.*, **55**, 2730–2747.
- Eldridge, R. H., 1958: A synoptic study of West African disturbance lines. *Quart. J. Roy. Meteor. Soc.*, **84**, 468–469.
- Evaristo, R., G. Scialom, N. Viltard, and Y. Lemaître, 2010: Polarimetric signatures and hydrometeor classification of West African squall lines. *Quart. J. Roy. Meteor. Soc.*, **136**, 272–288, doi:10.1002/qj.561.
- Fabry, F., and I. Zawadzki, 1995: Long-term radar observations of the melting layer of precipitation and their interpretation. *J. Atmos. Sci.*, **52**, 838–851.
- Faccani, C., and Coauthors, 2009: The impacts of AMMA radio-sonde data on the French global assimilation and forecast system. *Wea. Forecasting*, **24**, 1268–1286.
- Fink, A. H., D. G. Vincent, and V. Ermert, 2006: Rainfall types in the West African Sudanian zone during the summer monsoon 2002. *Mon. Wea. Rev.*, **134**, 2143–2164.
- Guy, N., and S. A. Rutledge, 2012: Regional comparison of West African convective characteristics: A TRMM-based climatology. *Quart. J. Roy. Meteor. Soc.*, **138**, 1179–1195, doi:10.1002/qj.1865.
- , —, and R. Cifelli, 2011: Radar characteristics of continental, coastal, and maritime convection observed during AMMA/NAMMA. *Quart. J. Roy. Meteor. Soc.*, **137**, 1241–1256, doi:10.1002/qj.839.
- Hamilton, R. A., J. W. Archbold, and C. K. M. Douglas, 1945: Meteorology of Nigeria and adjacent territory. *Quart. J. Roy. Meteor. Soc.*, **71**, 231–264, doi:10.1002/qj.49707130905.
- Houze, R. A., Jr., M. I. Biggerstaff, S. A. Rutledge, and B. F. Smull, 1989: Interpretation of Doppler weather radar displays of midlatitude mesoscale convective systems. *Bull. Amer. Meteor. Soc.*, **70**, 608–619.
- Janicot, S., and Coauthors, 2008: Large-scale overview of the summer monsoon over West Africa during the AMMA field experiment in 2006. *Ann. Geophys.*, **26**, 2569–2595.
- Johnson, R. H., and P. E. Ciesielski, 2000: Rainfall and radiative heating rates from TOGA COARE atmospheric budgets. *J. Atmos. Sci.*, **57**, 1497–1514.
- Klemp, J. B., and R. B. Wilhelmson, 1978: The simulation of three-dimensional convective storm dynamics. *J. Atmos. Sci.*, **35**, 1070–1096.
- Lafore, J.-P., J.-L. Redelsperger, and G. Jaubert, 1988: Comparison between a three-dimensional simulation and Doppler radar data of a tropical squall line: Transports of mass, momentum, heat, and moisture. *J. Atmos. Sci.*, **45**, 3483–3500.
- Laing, A. G., R. Carbone, V. Levizzani, and J. Tuttle, 2008: The propagation and diurnal cycles of deep convection in northern tropical Africa. *Quart. J. Roy. Meteor. Soc.*, **134**, 93–109, doi:10.1002/qj.194.
- Lang, S., W.-K. Tao, J. Simpson, and B. Ferrier, 2003: Modeling of convective–stratiform precipitation processes: Sensitivity to partitioning methods. *J. Appl. Meteor.*, **42**, 505–527.
- , —, —, R. Cifelli, S. Rutledge, W. Olson, and J. Halverson, 2007: Improving simulations of convective systems from TRMM LBA: Easterly and westerly regimes. *J. Atmos. Sci.*, **64**, 1141–1164.
- , —, X. Zeng, and Y. Li, 2011: Reducing the biases in simulated radar reflectivities from a bulk microphysics scheme: Tropical convective systems. *J. Atmos. Sci.*, **68**, 2306–2320.
- Laurent, H., N. D'Amato, and T. Lebel, 1998: How important is the contribution of the mesoscale convective complexes to the Sahelian rainfall? *Phys. Chem. Earth*, **23**, 629–633, doi:10.1016/S0079-1946(98)00099-8.
- Le Barbé, L., and T. Lebel, 1997: Rainfall climatology of the HAPEX-Sahel region during the years 1950–1990. *J. Hydrol.*, **188**, 43–73.
- Lebel, T., and Coauthors, 2010: The AMMA field campaigns: Multiscale and multidisciplinary observations in the West African region. *Quart. J. Roy. Meteor. Soc.*, **136**, 8–33, doi:10.1002/qj.486.
- Lerach, D. G., S. A. Rutledge, C. R. Williams, and R. Cifelli, 2010: Vertical structure of convective systems during NAME 2004. *Mon. Wea. Rev.*, **138**, 1695–1714.
- Liu, H., and V. Chandrasekar, 2000: Classification of hydrometeors based on polarimetric radar measurements: Development of fuzzy logic and neuro-fuzzy systems, and in situ verification. *J. Atmos. Oceanic Technol.*, **17**, 140–164.

- Lucas, C., E. J. Zipser, and B. S. Ferrier, 2000: Sensitivity of tropical West Pacific oceanic squall lines to tropospheric wind and moisture profiles. *J. Atmos. Sci.*, **57**, 2351–2373.
- Machado, L. A. T., J.-P. Duvel, and M. Desbois, 1993: Diurnal variations and modulation by easterly waves of the size distribution of convective cloud clusters over West Africa and the Atlantic Ocean. *Mon. Wea. Rev.*, **121**, 37–49.
- Mathon, V., H. Laurent, and T. Lebel, 2002: Mesoscale convective system rainfall in the Sahel. *J. Appl. Meteor. Climatol.*, **41**, 1081–1092.
- May, P. T., and T. P. Lane, 2009: A method for using weather radar data to test cloud resolving models. *Meteor. Appl.*, **16**, 425–432, doi:10.1002/met.150.
- Miller, M. A., and A. Slingo, 2007: The Arm Mobile Facility and its first international deployment: Measuring radiative flux divergence in West Africa. *Bull. Amer. Meteor. Soc.*, **88**, 1229–1244.
- Mohr, C. G., L. Jay Miller, R. L. Vaughan, and H. W. Frank, 1986: The merger of mesoscale datasets into a common Cartesian format for efficient and systematic analyses. *J. Atmos. Oceanic Technol.*, **3**, 143–161.
- Moncrieff, M. W., 1992: Organized convective systems: Archetypal dynamical models, mass and momentum flux theory, and parameterization. *Quart. J. Roy. Meteor. Soc.*, **118**, 819–850, doi:10.1002/qj.49711850703.
- Morrison, H., G. Thompson, and V. Tatarskii, 2009: Impact of cloud microphysics on the development of trailing stratiform precipitation in a simulated squall line: Comparison of one- and two-moment schemes. *Mon. Wea. Rev.*, **137**, 991–1007.
- Nicholls, S. D., and K. I. Mohr, 2010: An analysis of the environments of intense convective systems in West Africa in 2003. *Mon. Wea. Rev.*, **138**, 3721–3739.
- Parker, D. J., 2002: The response of CAPE and CIN to tropospheric thermal variations. *Quart. J. Roy. Meteor. Soc.*, **128**, 119–130, doi:10.1256/00359000260498815.
- , C. D. Thorncroft, R. R. Burton, and A. Diongue-Niang, 2005: Analysis of the African easterly jet, using aircraft observations from the JET2000 experiment. *Quart. J. Roy. Meteor. Soc.*, **131**, 1461–1482, doi:10.1256/qj.03.189.
- Payne, S. W., and M. M. McGarry, 1977: The relationship of satellite inferred convective activity to easterly waves over West Africa and the adjacent ocean during phase III of GATE. *Mon. Wea. Rev.*, **105**, 413–420.
- Penide, G., V. Giraud, D. Bouniol, P. Dubuisson, C. Duroure, A. Protat, and S. Cautenet, 2010: Numerical simulation of the 7 to 9 September 2006 AMMA mesoscale convective system: Evaluation of the dynamics and cloud microphysics using synthetic observations. *Quart. J. Roy. Meteor. Soc.*, **136**, 304–322, doi:10.1002/qj.558.
- Petersen, W. A., H. J. Christian, and S. A. Rutledge, 2005: TRMM observations of the global relationship between ice water content and lightning. *Geophys. Res. Lett.*, **32**, L14819, doi:10.129/2005GL023236.
- Powell, S. W., X. Zeng, R. A. Houze Jr., and W.-K. Tao, 2011: Heating rates of observed and simulated anvil clouds over Niamey. *Atmospheric System Research Science Team Meeting*, San Antonio, TX, U.S. Department of Energy.
- Protat, A., J. Delanoë, D. Bouniol, A. J. Heymsfield, A. Bansemir, and P. Brown, 2007: Evaluation of ice water content retrievals from cloud radar reflectivity and temperature using a large airborne in situ microphysical database. *J. Appl. Meteor. Climatol.*, **46**, 557–572.
- Redelsperger, J.-L., A. Diongue, A. Diedhiou, J.-P. Ceron, M. Diop, J.-F. Gueremy, and J.-P. Lafore, 2002: Multi-scale description of a Sahelian synoptic weather system representative of the West African monsoon. *Quart. J. Roy. Meteor. Soc.*, **128**, 1229–1257, doi:10.1256/003590002320373274.
- , C. D. Thorncroft, A. Diedhiou, T. Lebel, D. J. Parker, and J. Polcher, 2006: African monsoon multidisciplinary analysis: An international research project and field campaign. *Bull. Amer. Meteor. Soc.*, **87**, 1739–1746.
- Roberts, N. M., and H. W. Lean, 2008: Scale-selective verification of rainfall accumulations from high-resolution forecasts of convective events. *Mon. Wea. Rev.*, **136**, 78–97.
- Russell, B., and Coauthors, 2010: Radar/rain-gauge comparisons on squall lines in Niamey, Niger for the AMMA. *Quart. J. Roy. Meteor. Soc.*, **136**, 289–303, doi:10.1002/qj.548.
- Ruti, P. M., and Coauthors, 2011: The West African climate system: A review of the AMMA model intercomparison initiatives. *Atmos. Sci. Lett.*, **12**, 116–122, doi:10.1002/asl.305.
- Rutledge, S. A., and P. V. Hobbs, 1984: The mesoscale and microscale structure and organization of clouds and precipitation in midlatitude cyclones. XII: A diagnostic modeling study of precipitation development in narrow cold-frontal rainbands. *J. Atmos. Sci.*, **41**, 2949–2972.
- Schwendike, J., and S. C. Jones, 2010: Convection in an African Easterly Wave over West Africa and the eastern Atlantic: A model case study of Helene (2006). *Quart. J. Roy. Meteor. Soc.*, **136**, 364–396, doi:10.1002/qj.566.
- Scialom, G., and Y. Lemaître, 2011: Vertical moistening by AMMA mesoscale convective systems. *J. Atmos. Oceanic Technol.*, **28**, 617–639.
- Slingo, A., and Coauthors, 2008: Overview of observations from the RADAGAST experiment in Niamey, Niger: Meteorology and thermodynamic variables. *J. Geophys. Res.*, **113**, D00E01, doi:10.1029/2008JD009909.
- Soong, S.-T., and Y. Ogura, 1980: Response of tradewind cumuli to large-scale processes. *J. Atmos. Sci.*, **37**, 2035–2050.
- Steiner, M., R. A. Houze, and S. E. Yuter, 1995: Climatological characterization of three-dimensional storm structure from operational radar and rain gauge data. *J. Appl. Meteor.*, **34**, 1978–2007.
- Tao, W.-K., 2007: Cloud resolving modeling. *J. Meteor. Soc. Japan*, **85B**, 305–330.
- , and J. Simpson, 1993: The Goddard cumulus ensemble model. Part I: Model description. *Terr. Atmos. Oceanic Sci.*, **4**, 35–72.
- , and Coauthors, 2003: Microphysics, radiation and surface processes in the Goddard Cumulus Ensemble (GCE) model. *Meteor. Atmos. Phys.*, **82**, 97–137, doi:10.1007/s00703-001-0594-7.
- , and Coauthors, 2009: A multiscale modeling system: Developments, applications, and critical issues. *Bull. Amer. Meteor. Soc.*, **90**, 515–534.
- , S. W. Powell, P. Ciesielski, X. Zeng, R. A. Houze Jr., J. Yuan, and R. Johnson, 2011: Numerical simulations of the AMMA and TWP-ICE Mesoscale Convective Systems. *Atmospheric Research Science Team Meeting*, San Antonio, TX, U.S. Department of Energy.
- Tokay, A., A. Kruger, W. F. Krajewski, P. A. Kucera, and A. J. P. Filho, 2002: Measurements of drop size distribution in the southwestern Amazon basin. *J. Geophys. Res.*, **107**, 8052, doi:10.1029/2001JD000355.
- Tompkins, A. M., A. Diongue-Niang, D. J. Parker, and C. D. Thorncroft, 2005: The African easterly jet in the ECMWF Integrated Forecast System: 4D-Var analysis. *Quart. J. Roy. Meteor. Soc.*, **131**, 2861–2885, doi:10.1256/qj.04.136.

- Vanyve, E., N. Hall, C. Messenger, S. Leroux, and J.-P. van Ypersele, 2008: Internal variability in a regional climate model over West Africa. *Climate Dyn.*, **30**, 191–202, doi:10.1007/s00382-007-0281-6.
- Yuter, S. E., and R. A. Houze Jr., 1995: Three-dimensional kinematic and microphysical evolution of Florida cumulonimbus. Part II: Frequency distributions of vertical velocity, reflectivity, and differential reflectivity. *Mon. Wea. Rev.*, **123**, 1941–1963.
- Zawislak, J., and E. J. Zipser, 2010: Observations of seven African easterly waves in the east Atlantic during 2006. *J. Atmos. Sci.*, **67**, 26–43.
- Zeng, X., W.-K. Tao, S. Lang, A. Y. Hou, M. Zhang, and J. Simpson, 2008: On the sensitivity of atmospheric ensembles to cloud microphysics in long-term cloud-resolving model simulations. *J. Meteor. Soc. Japan*, **86A**, 45–65.
- , and Coauthors, 2009: A contribution by ice nuclei to global warming. *Quart. J. Roy. Meteor. Soc.*, **135**, 1614–1629, doi:10.1002/qj.449.
- , W.-K. Tao, T. Matsui, S. Xie, S. Lang, M. Zhang, D. O’C Starr, and X. Li, 2011: Estimating the ice crystal enhancement factor in the tropics. *J. Atmos. Sci.*, **68**, 1424–1434.